Full Articles

Physicochemical and functional peculiarities of metal oxide whiskers

E. A. Goodilin,[a,b]★ E. A. Pomerantseva,[a] D. A. Semenenko,[a] P. B. Kocherginskaya,[a] D. M. Itkis,[a] T. L. Kulova,[c] A. M. Skundin,[c] L. S. Leonova,[d] Yu. A. Dobrovol´skii,[d] M. N. Rumyantseva,[b] A. M. Gas´kov,[b] S. B. Balakhonov,[a] B. R. Churagulov,[b] and Yu. D. Tretyakov[a,b]

[a]*Materials Science Department, M. V. Lomonosov Moscow State University, 1 Leninskie Gory, 119992 Moscow, Russian Federation. Fax: +7 (495) 939 0998. E-mail: goodilin@inorg.chem.msu.ru*
[b]*Chemical Department, M. V. Lomonosov Moscow State University, 1 Leninskie Gory, 119992 Moscow, Russian Federation. Fax: +7 (495) 939 0998. E-mail: goodilin@inorg.chem.msu.ru*
[c]*A. N. Frumkin Institute of Physical Chemistry and Electrochemistry, Russian Academy of Sciences, 31 Leninsky prosp., 119991 Москва, Moscow, Russian Federation. Fax: +7 (495) 952 5308. E-mail: askundin@mail.ru*
[d]*Institute of Problems of Chemical Physics, Russian Academy of Sciences, 1 prosp. Akad. Semenova, 142432 Chernogolovka, Moscow Region, Russian Federation. Fax: +7 (496) 515 5420. E-mail: dobr@icp.ac.ru*

Practical aspects of preparation and prospects for practical use of a series of the metal oxide whiskers were studied. The procedures for the synthesis were proposed, and the phase composition, micromorphology, and electrochemical and sensor characteristics of the macroscopic (up to 5—10 mm long) whiskers in the Ba—V—O, Ba—Mn—O, and Sn—O systems were analyzed. The electroconducting $BaV_8O_{21-\delta}$ whiskers were prepared by the hydrothermal treatment. These whiskers possess stable electrochemical characteristics appropriate for the development of novel secondary current sources. The protonated form of the $Ba_6Mn_{24}O_{48}$ whiskers produced by the isothermal vaporization of chloride fluxes is a mixed conductor with the proton and electron conductivity at a level of mS units at 25 °C. A new procedure by the thermal disproportionation of tin(II) oxide under nitrogen was proposed for the growth of SnO_2 whiskers of various morphology. The produced whiskers have substantial sensor sensitivity toward a series of toxic components of the gaseous medium, such as nitrogen dioxide.

Key words: whiskers, transition metal oxides, cathodic materials, sensors.

Achievements of the modern inorganic chemistry form reliable basis for the creation of unique materials and their further practical use. In therecent time, the development of new procedures for the preparation of one-dimensional systems, namely, nanotubulenes, nanoribbons, and whiskers, becomes very significant. For example,

Published in Russian in *Izvestiya Akademii Nauk. Seriya Khimicheskaya,* No. 5, pp. 1023—1034, May, 2008.
1066-5285/08/5705-1042

vanadium oxides and their derivatives attract attention of researchers due to their special structure and properties. Among these systems, great attention is given to nanostructured materials, including "nanowires," "nanoribbons," "nanorods," and "nanowhiskers," [1,2] which are of doubtless practical interest for both fundamental research and potential use as sensors, cathodic materials, and others.[3,4]

The crystal structure of the $Ba_6Mn_{24}O_{48}$ phase has been found several years ago.[5] This structure represents a framework constructed due to the accretion of tunnels of different shape and size in which positively charged ions can be intercalated. Special interest to this compound is caused by a possibility of synthesizing this phase as long, flexible, and long crystalline fibers.[6] The procedures for the efficient insertion of protons and lithium into the whiskers and powdered samples of the $Ba_6Mn_{24}O_{48}$ phase have recently been proposed.[7–9]

Tin dioxide is one of the promising broad-band semiconductors with unique electric and optical characteristics, whose studies remained prospective for several decades.[10] Thin films of alloyed tin dioxide are widely used in transparent conducting electrodes[11] and solar batteries.[12] The sensors, whose sensitive elements are based on SnO_2, can find wide use as threshold sensors that react to the presence in atmosphere of toxic for human organism or dangerous gases, including CO, NO, NO_2, H_2, and others.[13] It is shown in several works that an increase in the ratio of the surface area to volume for the one-dimensional SnO_2 structures results in an appreciable change in the sensor sensitivity.[14] In the recent time, more studies are directed to investigation of various one-dimensional objects: nano- and microrods and whiskers of tin dioxide. The SnO_2 whiskers were prepared by sintering with NaCl,[15] by the hydrothermal method,[16] thermal decomposition,[17] fast oxidation method,[18] and thermal vaporization *in vacuo* or at temperatures higher than 1300 °C (see Refs 19—23).

The purpose of this work is to prepare macroscopic (up to several millimeters long) filamentary crystals (whiskers) based on vanadium, manganese, and tin oxides and to study their morphological and functional characteristics promising for practical use.

Experimental

Whiskers based on vanadium oxides were prepared by the hydrothermal treatment of barium-substituted xerogels of V_2O_5. The $V_2O_5 \cdot nH_2O$ gels were prepared by the interaction of crystalline vanadium(V) oxide with hydrogen peroxide according to a standard procedure.[24] The cherry-colored product was dried for ~6—7 h at ~50 °C. The xerogel plates were kept for 48 h in a saturated solution of $Ba(NO_3)_2$ for ion exchange and placed (under the distilled water layer) into a sealed Teflon tube mounted inside a steel autoclave, and the hydrothermal treatment was carried out at 200—250 °C for 8—48 h. As a result of the synthesis, yellow—green whiskers of various morphology were obtained. They were separated from the mother liquor, dried in air, and used for electrochemical measurements.

The chloride flux KCl ($T_m \approx 770$ °C) containing a specified quantity of the oxide blend (up to 50 wt.%) was used for the growth of whiskers in a Ba—Mn—O system. The mixture was heated to 800—1000 °C with a rate of 5 °C h^{-1} ($p(O_2) = 0.21$ atm) in the regime of isothermal vaporization of the solvent, stored for 2—10 days, and tempered in air. In order to prepare the H-form of whiskers, the whiskers were treated with 0.01, 0.1, 1, 10 *M*, and concentrated nitric acid for 1—10 days at room temperature and for 5—7 h at 65—75 °C with vigorous stirring on a magnetic stirrer containing a glass-ceramic heater. Further the whiskers were precipitated on a centrifuge, multiply washed at room temperature with distilled water until neutral pH was achieved, and dried in a drying oven at ~50 °C. The final product was the H-form of the considered phases of tunneling manganites.

The SnO_2 whiskers grew in a nitrogen flow containing the products of the thermal decomposition of SnO. To prepare SnO, commercial $SnCl_2 \cdot 2H_2O$ was dissolved in a minimum amount of hot HCl, and a saturated solution of Na_2CO_3 was added to pH > 7. The formed white precipitate of tin(II) oxohydrate was heated for 2—3 h under the mother liquor (at 110 °C) for the quantitative transformation of the oxohydrate into blue—black tin(II) oxide with metallic luster. The resulting product was thoroughly washed with distilled water and dried at 110 °C. An alundum boat with the SnO powder was placed in the hot zone of a tubular furnace (Nabertherm), which was purged with a nitrogen flow (100 mL min^{-1}). The temperature regime was experimentally optimized and consisted of two stages of isothermal storage: for 1 h at 350 °C and for 1 h at 1050 °C. Metallic plates of Sn and Pt were used in experiments. The plates were placed in a cooler zone, and the products precipitated on the boat walls and on the surface of the metallic plates.

The microstructure was studied and the chemical composition of the samples was monitored on a LEO SUPRA 50VP scanning electron microscope equipped with an autoemission source and an X-ray spectrometer for microanalysis (Inca, Oxford Instruments) at an accelerating voltage of 5—25 kV. Secondary electron images were obtained with magnification up to 200 000. The data of optical microscopy were obtained on a Nickon Eclipse E600 POL metallographic microscope. A STOE diffractometer (CuKα1 radiation (1.54183 Å), transmission geometry, increment by 2θ 0.01—0.03°, 2θ range 5—70°) and a Rigaku D/Max-2500 diffractometer with a rotating anode (Japan, CuKα1 radiation geometry (Bragg—Brentano geometry) increment by 2θ 0.05°, 2θ range 10—80°, recording in quartz cells without averaging rotation) were used for X-ray diffraction analysis. An FR-552 Guinier focusing camera was used to determine the lattice parameters (CuKα1 radiation, recording with a quartz crystal as a monochromator and germanium as internal standard). The lattice parameters were calculated using the standard program package for 10—15 reflections.

IR absorption spectra of the samples were recorded on a Perkin Elmer LLC Spectrum One spectrometer (USA) in the range from 400 to 8000 cm^{-1} with a scan increment of 4 cm^{-1}. The samples were molded into pellets 13 mm in diameter with spectrally pure KBr (molding force 4 t, pressure ~300 MPa) based on 0.1—1 mg of the powder per 100 mg of KBr. The spectra were analyzed according to literature data.

The lithium content in the samples was determined by atomic emission spectroscopy with inductively-coupled plasma (ICP)

on a Perkin Elmer Optima 5300 spectrometer (power of the plasma burner 1350 V, argon (99.998%) pressure ~8.57 atm (120 psi), sample feed rate 2 mL s^{-1}). To prepare solutions, a weighed sample was dissolved in nitric acid with the addition of hydrogen peroxide. The nitric acid multielement standard (Perkin Elmer Optima Family) was used as the standard.

To evaluate the ability of the materials under study to electrochemical processes of lithium insertion and extraction, electrodes were prepared and studied in traditional electrochemical cells. The active mixture for the working electrodes was prepared by mixing of 75% active material, 20% additive for enhancing the electroconductivity (acetylene carbon black), and 5% binding (poly(vinylidene difluoride) dissolved in *N*-methylpyrrolidone) followed by homogenation on an UZDN-4D ultrasonic disperser. The prepared active mixture was deposited with a spatula on the both sides of the current feeder of a nickel network with a thickness of 0.05 mm. To remove *N*-methylpyrrolidone, the electrodes were dried for 5 h in a drying oven at 90 °C. After this the electrodes were pressed under a pressure of 500 kg cm^{-2} for 30 s. Then the electrodes were repeatedly dried *in vacuo* at 120 °C for 8 h to remove water traces. The amount of the active substance on the electrodes 1.5S1.5 cm in size was, as a rule, 7—10 mg. The counter and reference electrodes were prepared by rolling thin strips of lithium (LE-1 trade mark) of a certain thickness on a nickel network with the welded current feed of a nickel foil.

The electrodes were tested (charge—discharge curves and cyclic voltammograms were recorded) in sealed Teflon electrochemical cells containing one working electrode, two counter electrodes, and the reference electrode. All electrodes were separated by separators of porous polyprolylene (trade mark PORP (NPO Ufim, Moscow). Such cells rather well imitate the conditions of functioning of galvanic cells. All procedures on cell assembling were carried out in a dry box under an argon atmosphere. The electrolyte used was the standard electrolyte produced at the OAO Litii-element (Saratov, Russia), being a 1 *M* solution of $LiClO_4$ in a mixture of propylene carbonate (PC) and dimethoxyethane (DME) (7 : 3). The water content in these electrolytes measured by the Fischer method (684 KF-Coulometer, Metrohm, Switzerland) was at most 50 ppm.

Galvanostatic charge—discharge curves were recorded using a multichannel computerized setup for cycling produced at the OAO Buster (St. Petersburg, Russia). The models were cycled in the potential interval of the positive electrode 1.5—4.0 V at 20 °C. The current density during cycling was 20 mA per 1 g of the studied substance, which corresponds to 0.031—0.045 mA cm^{-2}. Cyclic voltammograms (CV) were recorded on an EL-2 potentiostat designed and produced at the A. N. Frumkin Institute of Physical Chemistry and Electrochemistry (Russian Academy of Sciences, Moscow, Russia). The potential sweep rate was 0.13 mV s^{-1}. For X-ray diffraction studies, the electrodes after polarization were thoroughly washed with neat dimethoxyethane from electrolyte residues and dried over P_2O_5. All procedures, beginning from cell dismantling, were carried in a dry box under an argon atmosphere.

The electrochemical system consisting of a PS-7 potentiostat and a Z-350M impedance meter (Elins) with automated computer detection was used to study the proton conductivity. To reveal a possibility of proton transfer, we carried out the study with symmetric electrochemical cells with ionic filters based on ammonium heteropolytungstate $(NH_4)_2HPW_{12}O_{40} \cdot nH_2O$ ($n \approx 12$): $Pt_{sponge}/(NH_4)_2HPW_{12}O_{40} \cdot 12\ H_2O/H^+$-whiskers/$(NH_4)_2HPW_{12}O_{40} \cdot 12\ H_2O/Pt_{sponge}$ (Pt_{sponge} is platinum sponge).

A ionic filter represented a protonic solid electrolyte (SEL) with the ion component of conductivity about $3 \cdot 10^{-2}$ S cm^{-1} and the electron component less than 10^{-8} S cm^{-1}. Exchange currents between the protonated whiskers and proton-conducting electrolyte were calculated by an analysis of the impedance locus of the cell: Pt_{sponge}/H^+-whiskers/$(NH_4)_2HPW_{12}O_{40} \cdot 12\ H_2O/H^+$-whiskers/$Pt_{sponge}$.

Four-electrode electrochemical cells with ionic and electronic potential probes were used for the quantitative separation of the ion and electron components, respectively, of the conductivity of the protonated $Ba_6Mn_{24}O_{48}$ phase.

The sample of the protonated $Ba_6Mn_{24}O_{48}$ phase was pressed under a pressure of $2 \cdot 10^3$ kg cm^{-2} into a cylindrical Teflon ring; layers of the solid electrolyte and platinum sponge were consequently pressed under the same pressure to the sample from the both sides. Finally, the whole structure was clutched by titanium punches, which were simultaneously used as current feeders: $Ti/Pt_{sponge}/(NH_4)_2HPW_{12}O_{40} \cdot nH_2O/H^+$-ceramics/$(NH_4)_2HPW_{12}O_{40} \cdot nH_2O/Pt_{sponge}/Ti$.

To produce potential electrodes (probes) in the central part of the Teflon ring, whose inner side contacts with the ceramic sample under study, three holes 2 mm in diameter were drilled by vertical, and first the H^+-SEL layer and then the platinum layer were pressed in them, which corresponded to the Pt/H^+-SEL/ceramics semielement. The distance between the centers of these holes was taken as a distance between the electrodes. Electrodes reversible by hydrogen were chosen as reversible current electrodes. When studying the electron conductivity, we measured the volt—ampere characteristic between the potential Ni electrodes (probes) pressed uniformly along the height of the studied ceramic samples in the cell: Ti/ceramics under study/Ti, and titanium punches served as current electrodes.

The sensor sensitivity was determined by the results of measurements of the electroconductivity at a constant current strength in artificial air and gas mixtures of specified composition. The whiskers were deposited on a chip with a platinum heater and gold contacts. The samples consisting of a whisker bundle were fixed on the contacts with a conducting paste based on metallic silver. The gas mixture with a specified NO_2 concentration was created by a GDP-102 dynamic flow generator using a microflow source of the gas containing NO_2 with the calibrated bulk flow $G_H = 4.61$ μg min^{-1}. The change in the NO_2 concentration in the gas mixture was achieved due to the variation of the carrier gas (synthetic air) flow in the interval 100—1200 mL min^{-1}. To create specified stable gas flows, electronic blocks for gas flow formation (GFF) were used. The NO_2 concentrations were calculated by the formula

$$C - G_H/Q \cdot 103,$$

where C is the mass concentration (mg m^{-3}), G_H is the bulk flow (mg min^{-1}), and Q is the carrier gas consumption (mL min^{-1}); $Q = 1200$ mL min^{-1} corresponds to $C_{NO_2} = 2$ ppm. The units (milligram per cubic meter) were recalculated to other units (ppm) by the Mendeleev—Clapeyron equation.

Results and Discussion

Whiskers based on vanadium oxides

The synthesis of microcrystals and nanoribbons of vanadium bronzes is widely discussed in the literature.[1–4] However, procedures for the formation of larger crystals (macroscopic "whiskers") are absent. The morphology of the whiskers prepared in this work is shown in Figs 1—5. After the hydrothermal treatment, the crystal samples were nanodimensional filaments and complex microstructures formed from such filamentary crystals (see Fig. 1). According to the X-ray diffraction data, the resulting whiskers up to 3 mm long and with the thickness much less than 1 μm had the layered crystal structure (Fig. 6) and predominant packing (texture), indicating that their morphology is similar to that of the nanoribbons. According to the energy dispersive X-ray (EDX) microanalysis data, the whisker composition is close to $BaV_8O_{21-\delta}$.

The charge—discharge curves of the $BaV_8O_{21-\delta}$ electrode are presented in Fig. 7. The initial discharge capacity of $BaV_8O_{21-\delta}$ was ~175 mA h g^{-1}. In the second cycle, the capacity decreased to 138 mA h g^{-1}, which is characteristic of the vanadium oxide electrodes and due to irreversible processes that occur upon the primary electrode polarization. Two areas corresponding to lithium insertion and a decrease in the oxidation state of vanadium are well discernible in the cathodic part of the charge—discharge curve. One prolonged area, reflecting lithium extraction from $BaV_8O_{21-\delta}$ and an increase in the oxidation state of vanadium, is detected in the anodic part of the charge—discharge curve. The cyclic voltammograms of the $BaV_8O_{21-\delta}$ electrode show two peaks at potentials of 2.77 and 2.44 V in the cathodic part of the curve. The response peaks at potentials of 2.74 and 3.03 V are detected in the anodic part of the curve. The peaks in the CV curve (as well as the areas in the charge—discharge curves) reflect the insertion process (cathodic peaks) and lithium extraction (anodic peaks). The difference between the anodic peak potential and the potential of the corresponding cathodic peak is 0.25 V for the first peak and 0.30 V for the second peak.

This difference between the potentials is characteristic of intercalation materials. The discharge capacity calculated from the cyclic voltammogram was 165 and 156 mA h g^{-1} for the first and second cycles, respectively, which agrees with the results of galvanostatic cycling. The discharge capacity equal to 156 mA h g^{-1} corresponds to the insertion, on the average, of 5.13 lithium atoms per $Li_{5.13}BaV_8O_{21-\delta}$ molecule (*i.e.*, 0.64 lithium atom per vanadium atom), and the oxidation state of vanadium changes from +5 to +4.36. The change in the discharge capacity of the $BaV_8O_{21-\delta}$ electrode during galvanostatic cycling indicates that the capacity is stable and remains virtually unchanged from the second to 20th cycle, which is especially important for practical use of these materials in lithium accumulators. If the whiskers are dried under the dynamic vacuum conditions (dehydrogenation) at 150—200 °C, then the capacity at the third cycle decreases only by 10—15% and remains at a level of 500—520 mA h g^{-1}.

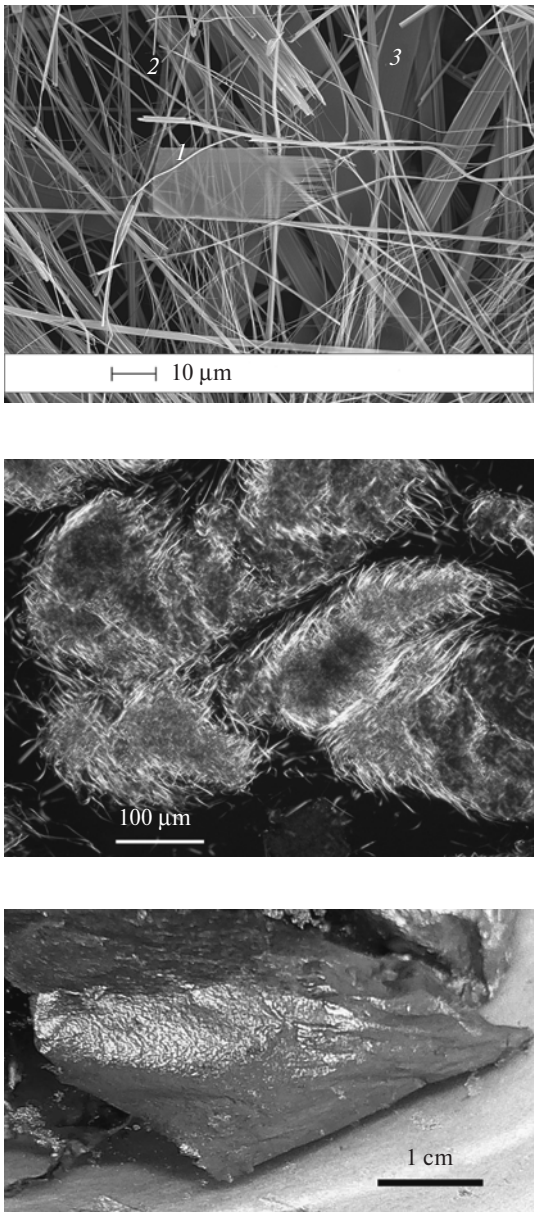

Fig. 1. Microphotograph of the $BaV_8O_{21-\delta}$ whiskers prepared by the hydrothermal synthesis: (*a*) scanning electron microscopy data: *1*, planar nanostructure transparent for electron beam; *2*, whiskers with the diameter less than 100 nm; *3*, large accretions of whiskers; (*b*) data of optical microscopy and (*c*) general view of the conducting "paper" prepared by drying of the whisker layer.

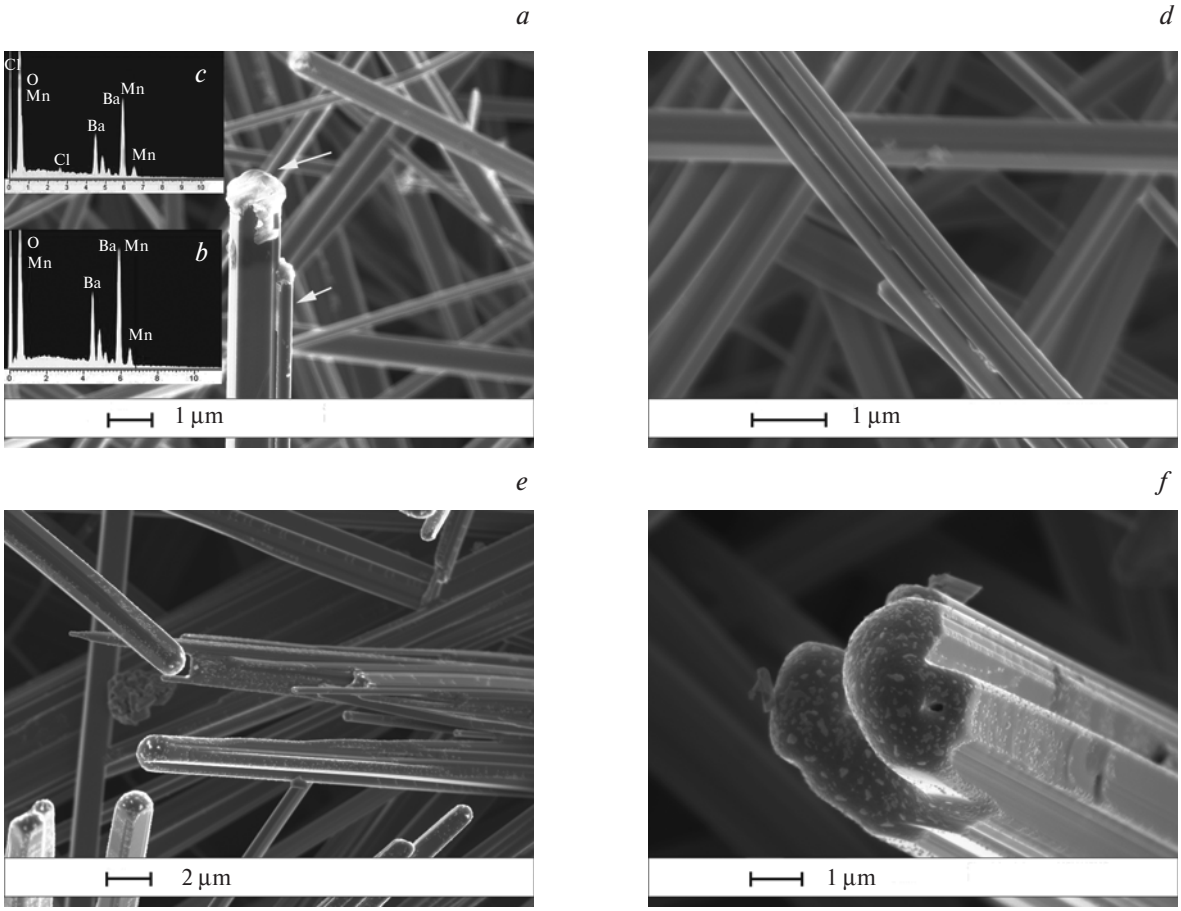

Fig. 2. Morphology of growth of the $Ba_6Mn_{24}O_{48}$ whiskers: *a*, whisker with a drop of the solidified flux on the whisker top; *b*, EDX spectrum obtained for the central part of the whisker (Ba : Mn = 8.2 : 28.1 ≈ 1 : 3.4, no potassium or chlorine was observed); *c*, EDX spectrum obtained for a drop on the whisker top (Ba : Mn : Cl = 10.4 : 22.8 : 4.8); *d*, typical view of the medium part of the whisker formed by the accretion of thinner whiskers; residues of the congealed flux are seen in the accretion sites; *e*, round bottom part (base) of the whisker contacting with the initial $BaMnO_3$ pellet; *f*, magnified image of the whisker base.

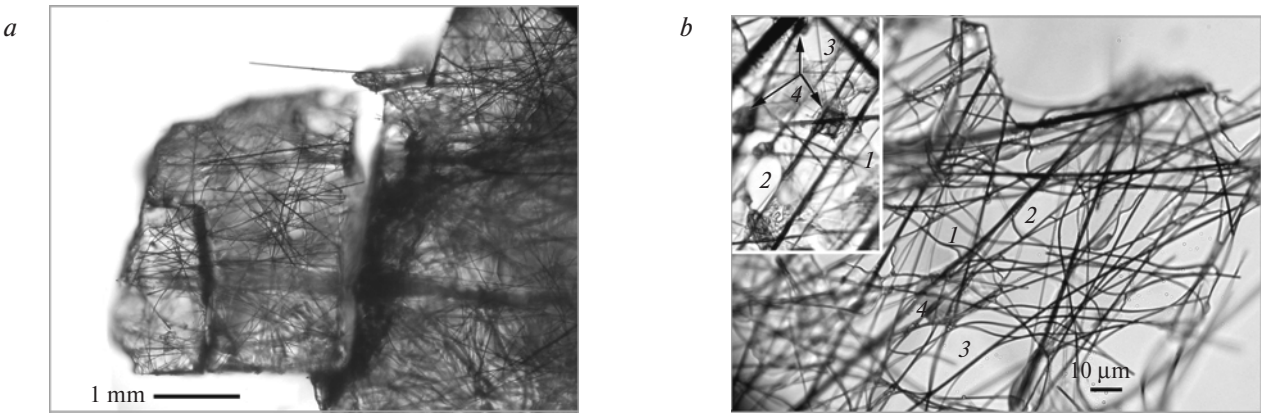

Fig. 3. Interaction of growing whiskers and chloride fluxes (optical microscopy): (*a*) general view of the whiskers growing in a transparent melt/KCl crystal; (*b*) whiskers in a thin wedge of the solidified melt under large magnification: *1*, layer of a solidified KCl melt; *2*, holes formed in the thin residual layer of a KCl melt due to vaporization; *3*, whiskers; *4*, colored (green—blue) crystallites in the melt (magnified fragment is given in inset).

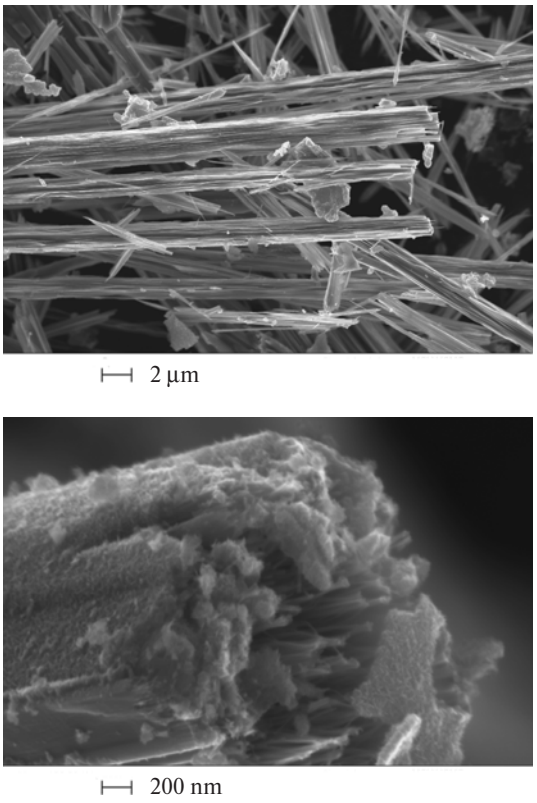

Fig. 4. Morphology of the H-form of whiskers of the $Ba_6Mn_{24}O_{48}$ phase prepared by the treatment with concentrated nitric acid at 65 °C for 5 h: (*a*) general view of the crystals and (*b*) formation of nanowhiskers at the edge of a particular crystal.

Whiskers based on manganese oxides

Whiskers of the $Ba_6Mn_{24}O_{48}$ phase, needle-like crystals of the $Ba_{2-x}Mn_{8-y}O_{16}$ hollandite, or their mixture were obtained reproducibly and in high yield by the isothermal vaporization of the chloride fluxes (KCl, NaCl, or their eutectic mixture) in the Ba—Mn—O system, depending on the temperature of synthesis (see Figs 2 and 3). The both phases (hollandite $Ba_{2-x}Mn_{8-y}O_{16}$ and the $Ba_6Mn_{24}O_{48}$ phase) exist in the region enriched in manganese(IV) oxide and are characterized by relatively small homogeneous regions by barium. However, the thermal stabilities of these phases differ substantially. The optimum temperature of crystal growth of the $Ba_6Mn_{24}O_{48}$ phase from KCl in air is 950—960 °C. An admixture of hollandite needles was always observed at temperatures T < 900 °C, whereas hausmannite Mn_3O_4 is formed at $T >>$ 950 °C. The crystal growth of the $Ba_6Mn_{24}O_{48}$ phase is favored by the use of the barium-enriched blend, and the crystals grow better when the oxide blend is used as densely molded and pre-annealed pellets placed in a melt of the isothermally vaporizing chloride flux. The needles grow on the external surface of the pellet forming a "felt,"

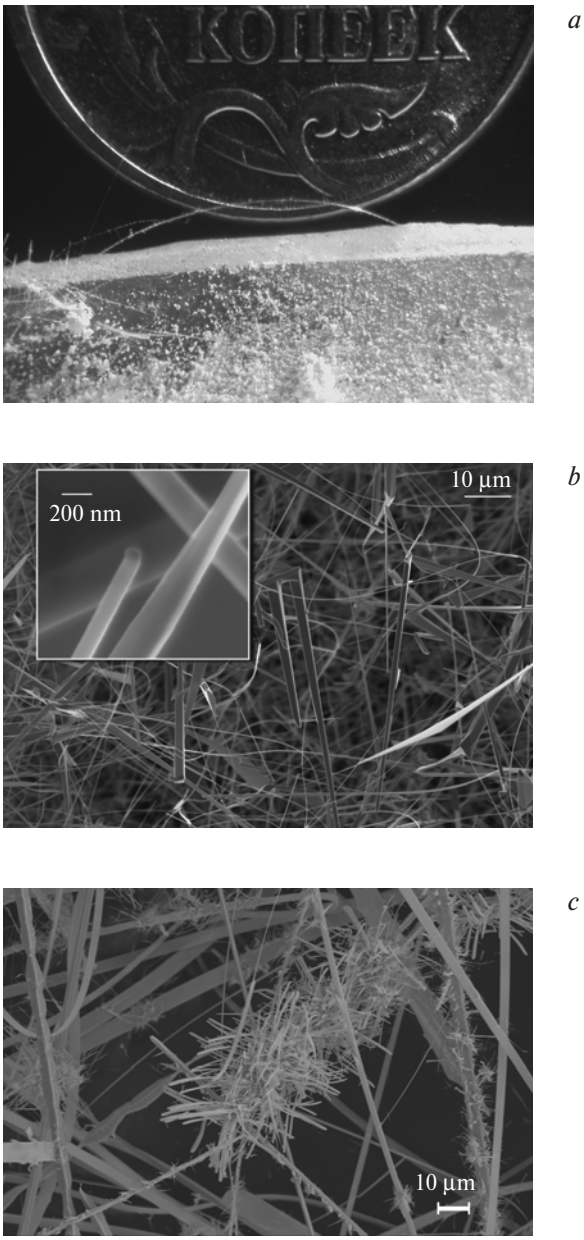

Fig. 5. Morphology of the SnO_2 whiskers: (*a*) general view of the whiskers in the grow the boat and the optical microphotograph of the SnO_2 whisker about 2 cm long against the background of a five-kopeck coin; (*b*) microphotograph of the samples synthesized in experiments with the platinum support; inset, an image of a whisker with the congealed drop on the end; (*c*) microphotograph of the samples synthesized in the presence of metallic tin.

which is easily separated mechanically, and the unreacted reactants and admixture phases (Mn_2O_3, Mn_3O_4, *etc.*) remain in the major bulk of the pellet. Flux vaporization solves an important problem of separation of the prepared crystals from the solvent, which is usual for the standard method of crystal growth from solution in melt. According to the EDX data, the whiskers are crystals with the

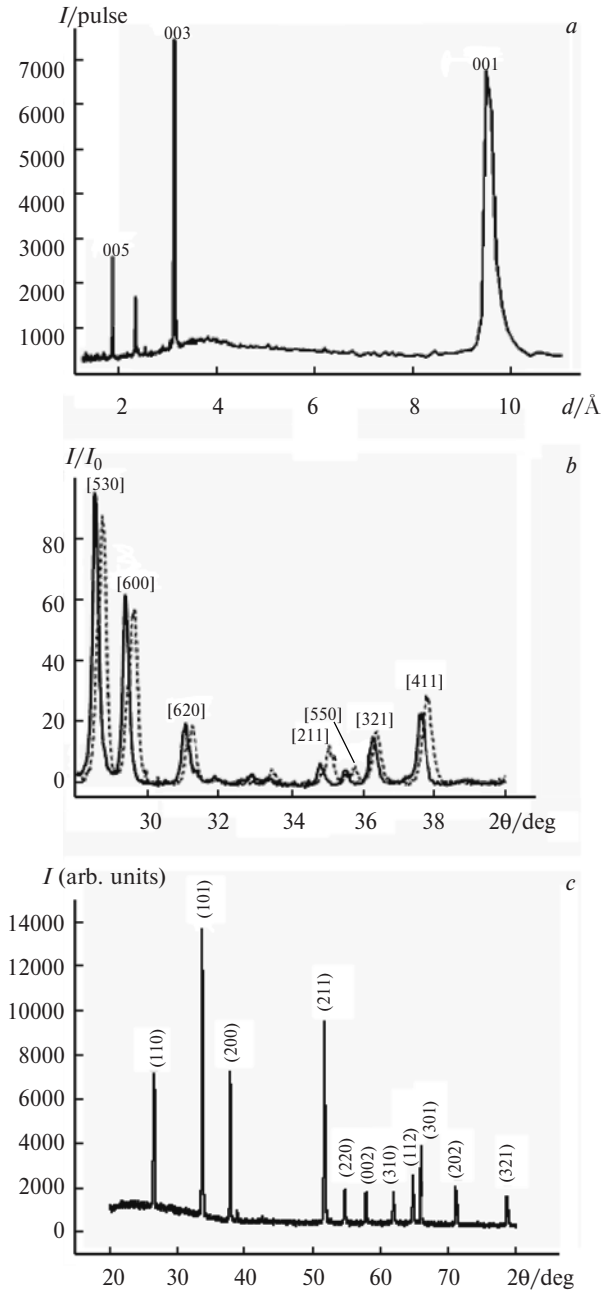

Fig. 6. X-ray diffraction data for whiskers: (*a*) $BaV_8O_{21-\delta}$ whiskers with the designation of the main peaks composing the series 00l, (*b*) diffraction patterns of the samples of the initial (solid line) and protonated (dotted line) $Ba_6Mn_{24}O_{48}$ phase, and (*c*) X-ray pattern of the SnO_2 whiskers.

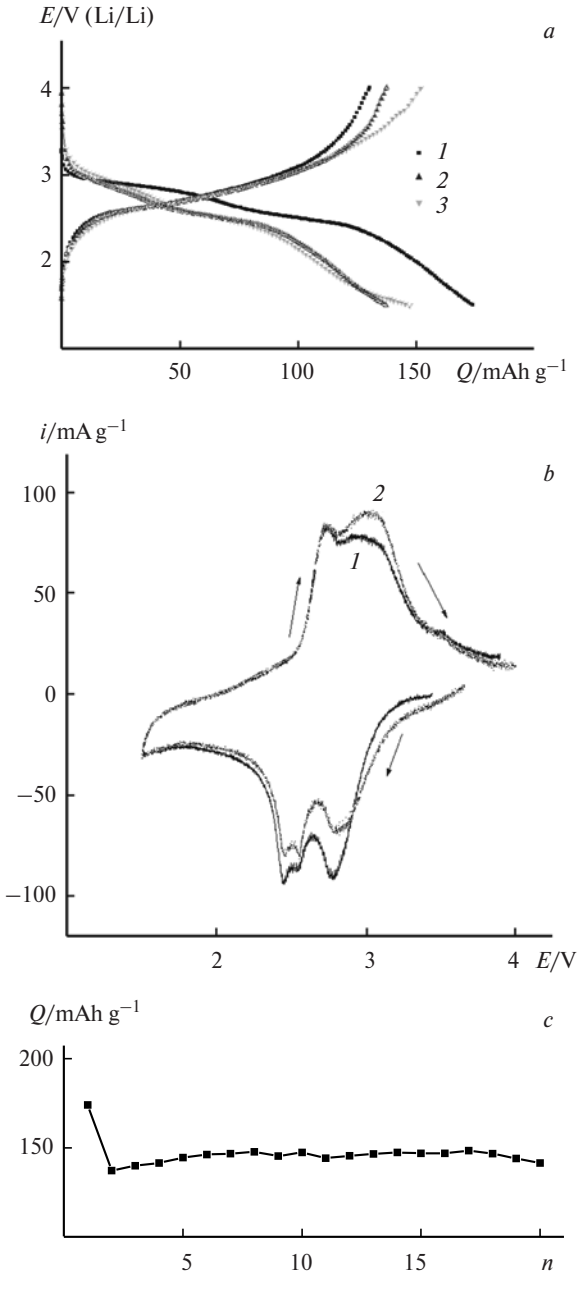

Fig. 7. Electrochemical characteristics of the $BaV_8O_{21-\delta}$ whiskers (electrolyte 1 *M* $LiClO_4$ in a PC—DME (7 : 3) mixture; *1*, cycle 1; *2*, cycle 2; *3*, cycle 10: (*a*) charge—discharge curves of the $BaV_8O_{21-\delta}$ electrode, current density 20 mA g^{-1}, (*b*) cyclic voltammograms of the $BaV_8O_{21-\delta}$ electrode, potential sweep rate 0.13 mV/s, and (*c*) change in the discharge capacity of the $BaV_8O_{21-\delta}$ electrode during cycling, current density 20 mA g^{-1}.

chemically homogeneous composition in which the content of potassium and chloride does not exceed 1 at.% (for example, Ba : Mn : O : K : Cl = (7.4—7.6) : (25.0—27.5) : (64.6—67.0) : (0—0.3) : (0—0.6) for a series of points analyzed with an increment of 2—4 μm on the whisker accretion with a thickness of 3—4 μm).

The whiskers of the $Ba_6Mn_{24}O_{48}$ phase can be divided into two types: thicker freely standing whiskers growing on the pellet surface (see Fig. 2) and thinner single whiskers growing in the chloride flux layer (see Fig. 3). Whiskers, as a rule, form bundles consisting of thinner nanofibers

oriented in one direction. In addition, rather bulky "pseudosingle crystals," as well as dendrites and "bushes," are met. One also can prepare a large amount of very thin, long, and flexible fibers of the $Ba_6Mn_{24}O_{48}$ phase with a diameter of 0.1—1 μm and a ratio of the length to diameter of 10^4—10^5 and those reaching a length of several millimeters. Such fibers are formed on the surface of the chloride flux, which is transformed into the felt-like layer 1—2 mm thick consisting of the twisted bent $Ba_6Mn_{24}O_{48}$ whiskers (see Fig. 3). The latter can easily be separated mechanically from a pellet.

Peculiarities of the growth of the $Ba_6Mn_{24}O_{48}$ whiskers are shown in Fig. 2. These data indicate that the whiskers are formed *via* the mechanism relative to the vapor—liquid—crystal (VLC) mechanism. The EDX data show that drops of nonvolatile $BaCl_2$ are formed on the top of the crystals. Nevertheless, these drops are not strongly localized on the whisker tops and can flow down or, on the contrary, rise by the capillary forces along the lateral crystal surface, resulting in accretions of codirectly growing whiskers. Probably, the nonvolatile components of the melt (*e.g.*, $BaCl_2$) can also be localized at the juncture site: in a region of the dihedral angle between the planar surface of a thicker whisker and the top of a thinner whisker sliding along the planar surface during the growth time.

At the same time, several facts do not allow one to explain completely the growth of the $Ba_6Mn_{24}O_{48}$ whiskers by the classical VLC mechanism. First, the $BaCl_2$ drops should rapidly be consumed during the crystal growth, because this is the only source of barium in the system, so that the formation of long whiskers becomes impossible. Second, the whiskers are well wet with a chloride melt; however, according to the classical VLC mechanism, the wetting should be sufficiently weak for a catalyst drop to remain stable. Third, along with the freely standing whiskers, there is a fraction of "floating" whiskers that form a layer on the chloride melt surface. They can also be observed in the solidified layer of the chloride melt even at a distance of 1 cm from the reactant pellet placed in the flux (see Fig. 3). These whiskers are completely immersed into the melt and, hence, we cannot believe that they grow only due to the "catalyst" drops on their tops. The studies show that the most part of whiskers grow due to the extrusion of the crystals from their base (pedestal mechanism). Probably, three phases should be involved in the formation of the $Ba_6Mn_{24}O_{48}$ whiskers: gas (O_2 that oxidizes $MnCl_2$ to the oxide phases), liquid ($BaCl_2$), and solid (whisker). At the same time, crystal growth can involve a single catalyst drop for each whisker and also due to a localized center enriched with barium chloride, resulting in the growth of thick pseudosingle-crystalline, freely standing, and oriented in one direction whiskers or a layer of whiskers floating on the chloride melt surface.

The X-ray diffraction analysis of the H-form of the $Ba_6Mn_{24}O_{48}$ phase (see Fig. 6) shows that all major reflections characteristic of the initial structure are retained and the material undergoes no appreciable amorphization. The unit cell parameters for a sample of the $Ba_6Mn_{24}O_{48}$ phase obtained by storing in concentrated nitric acid at room temperature for 7 days are $a = 18.033(6)$ Å, and $c = 2.833(1)$ Å, *i.e.*, the a parameter of the initial phase changes substantially (by ~0.15 Å), whereas the c parameter remains unchanged. Such a high value of changing the a parameter is due, most likely, to the removal of the barium ions with the large ionic radius from the structure. According to the data of EDX microanalysis and atomic emission spectroscopy with inductively-coupled plasma, the barium content in the H-form of the $Ba_6Mn_{24}O_{48}$ phase decreases by ~30 at.% compared to the starting phase. Second, the decrease in the a parameter is a consequence of an increase in the average oxidation state of manganese from 3.5 to 3.8—3.9 (according to iodometric titration). Similar phenomenon is observed for the extraction of alkaline metal ions from hollandite[25] and lithium—manganese spinels,[26,27] and the commonly accepted mechanism that explains this process is the disproportionation of Mn^{III} to Mn^{IV} remaining in the tunnel walls and Mn^{II} that transfers into the solution. Indeed, an analysis of the chemical composition of the solution obtained by the formation of the H-form of the $Ba_6Mn_{24}O_{48}$ phase shows that the solution contains both the barium and manganese ions in the ratio Ba : Mn ≈ 1 : 1.5, which excludes the congruent dissolution of the phase in nitric acid and also indicates that the protonation process can be restricted by a simple ion exchange accompanied by washing out of the barium ions to the solution. Thus, defects are formed in the tunnel walls of the $Ba_6Mn_{24}O_{48}$ phase. The defects represent the absent manganese atom and a portion of oxygen coordinately bound to it. In this case, the nearest coordination environment of the manganese ions around the defect is likely distorted.

According to the IR spectra data, the protons in the structure are fixed due to the formation of the Mn—O—H bonds. Vibrations at ~1100 cm^{-1} (Fig. 8), according to published data, are most intense in the IR spectra of manganites and favor bending vibrations of the OH groups bound to manganese.[28] Independent structural studies show that this is the hydroxyl that exists in the material bulk. The IR spectrum (see Fig. 8) also exhibits a line at 3000—3500 cm^{-1} corresponding to stretching vibrations of the OH groups bound to manganese in manganites.

The protons of the Mn—OH bond in tunneling and layered manganese oxides are very labile, which results, in some cases, in the appearance of a significant proton conductivity (Figs 9 and 10). Investigation on the symmetric electrochemical cells was carried out to study a possibility of proton transfer in the protonated $Ba_6Mn_{24}O_{48}$ whiskers. The cyclic voltammograms (see Fig. 9) demonstrate the dependence of the current on both the potential sweep rate and hydrogen content in the gas phase. In the

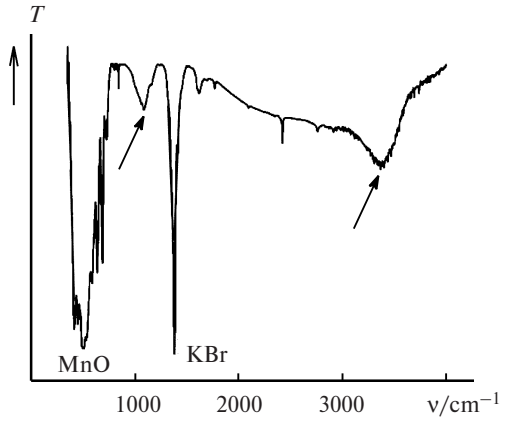

Fig. 8. IR spectrum of the H-form of the $Ba_6Mn_{24}O_{48}$ phase prepared by keeping in concentrated HNO_3 for 15 days. Arrows mark lines in a region of ~1100 cm^{-1} corresponding to the bending vibrations of the OH groups and lines at ~3500 cm^{-1} belonging to stretching vibrations of the OH groups. The vibrations of the lattice Mn—O groups and residual line of the KBr matrix are also designated.

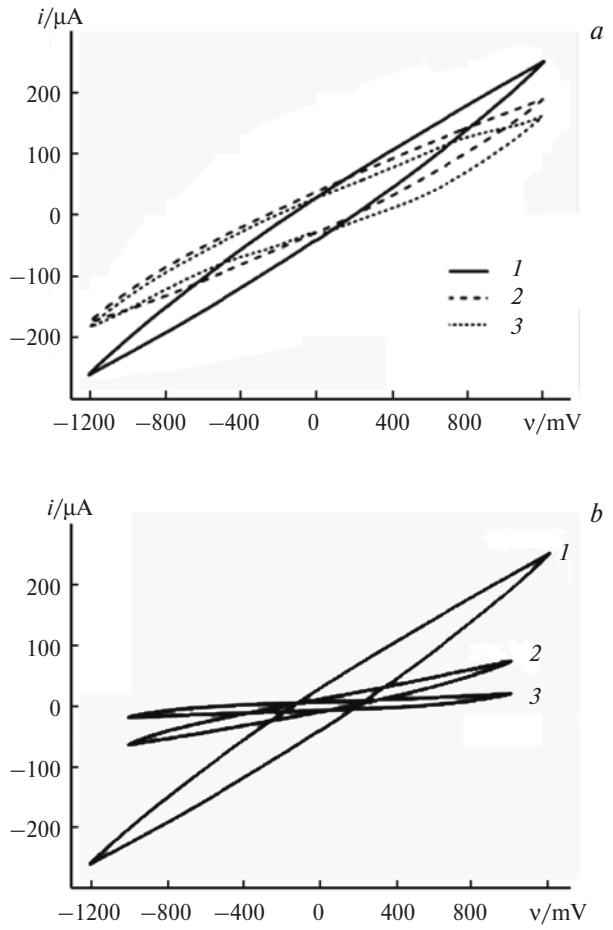

Fig. 9. Plots of the voltammograms of the $Pt_{sponge}/(NH_4)_2HPW_{12}O_{40} \cdot 12H_2O/H^+$-whiskers/$(NH_4)_2HPW_{12}O_{40} \cdot 12H_2O/Pt_{sponge}$ electrochemical cell (*a*) *vs* rate of potential application (50% H_2, air, T = 24 °C, relative humidity 25%): 400 (*1*), 100 (*2*), and 20 mV s^{-1} (*3*); (*b*) *vs* gaseous medium composition at a fixed rate of potential (400 mV s^{-1}) application: *1*, 50% H_2; *2*, 5% H_2; *3*, 100% air.

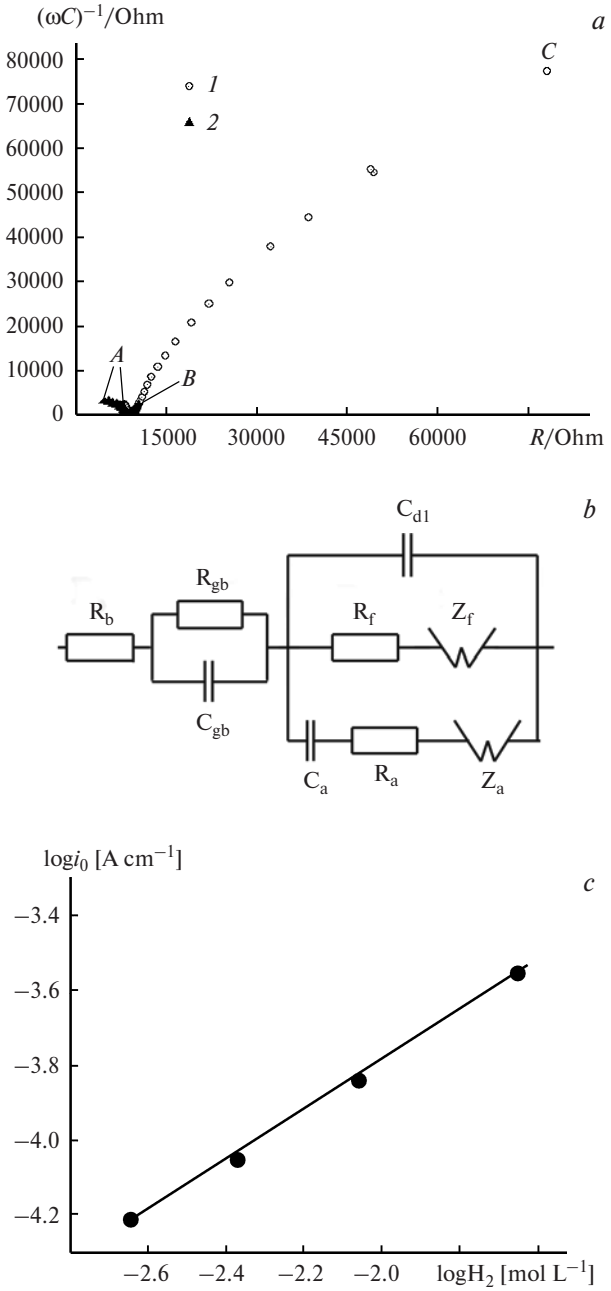

Fig. 10. Impedance spectroscopy of the protonated magnetic whiskers: (*a*) impedance spectra in various media (T = 24 °C, relative humidity 58%, spectra recording by the two-electrode scheme between the current electrodes): *1*, 100% air; *2*, 50% air—50% H_2 mixture; *A*, 10^6 Hz; *B* and *C*, 0.1 Hz; (*b*) equivalent scheme; (*c*) experimental dependence of the exchange currents on the gas phase composition.

both cases, the cyclograms demonstrate hysteresis phenomena, especially under an atmosphere with a high hydrogen content. This type of cyclic volt—ampere characteristics and the values of currents passing through the cell indicate a considerable contribution of the proton conductivity to the overall conductivity of the whiskers complicated by the retarded diffusion. A substantial depen-

dence of the volt—ampere characteristics on the hydrogen concentration in the gas phase can also indicate that the resistance at the electrode boundaries contributes to the ion chains, which shunts the electron conductivity.

The impedance spectra obtained by the two-electrode scheme are complicated. However, their shape (see Fig. 10) depends on the hydrogen concentration in the gas phase. The equivalent scheme describing the impedance spectrum includes the resistance at the boundaries with the electrodes (R_b), contribution of the intercrystallite boundaries (*gb*), and ion, electron, and diffusion components. The four-probe method was used for the quantitative determination of the electron and ion components. When measuring the ion component of the conductivity, we measured the change in time of the potential between the electrodes after galvanostatic pulse application between the current electrodes. The specific conductance (conductivity) was determined after the potential reached a constant value. The measurements were carried out at different galvanostatic pulses. The use of this regime and measurements on the samples of different thickness made it possible to exclude the influence of the current of binary layer charging, which contributes to the initial period after potential application. An analysis of the time dependence between the potential electrodes after the application of galvanostatic pulses of different value in air and in an atmosphere containing hydrogen shows that a constant emf value is established within ~30 s and the resistance is proportional to the current and sample thickness, indicating no substantial contribution of the boundary resistance. The composition of the environment (air and air—oxygen mixture) exerts a weak effect on the measured resistance value. The ion conductivity calculated by the results of measurements is $(9.9\pm0.5)\cdot10^{-4}$ $Ohm^{-1}\,cm^{-1}$. When measuring the electron component of the conductivity, three potential electrodes were used to determine the dependence of the resistance on the sample thickness. The voltammograms obtained in the cell for measuring the electron conductivity has a purely ohmic character, and the determined resistance values are rigidly proportional to the ceramic thickness. The specific electron conductance of the ceramics at 24 °C was $(8.30\pm0.02)\cdot10^{-4}$ $Ohm^{-1}\,cm^{-1}$. Thus, the $Ba_6Mn_{24}O_{48}$ whiskers and their protonated H-form can find use as electrochemically active reinforcing filaments to improve the mechanical characteristics of flexible cathodic materials and proton-conducting polymers. Due to their "felt-like" structure, the $Ba_6Mn_{24}O_{48}$ whiskers can act as efficient electrode materials for gas-permeable fuel cells or gas sensors.

Whiskers based on tin dioxide

The typical morphology of the tin dioxide whiskers prepared in the present work by the growth in the optimized regime is shown in Fig. 5. According to the X-ray diffraction data (see Fig. 6), the SnO_2 whiskers are classified as the tetragonal modification of SnO_2 (PDF-2 card no. 77-447). The isothermal vaporization of SnO in the standard regime, which consists of heating to 1050 °C with a rate of 10 °C min^{-1} followed by storing at this temperature for 1 h in a nitrogen flow, results in the precipitation of a white powder on the boat walls. However, the amount of the grown whiskers in these experiments is negligible. To enhance the whisker yield, the temperature regime was optimized by the additional storage at 250—400 °C. The optimum regime turned out to be the crystal growth at 1050 °C with the preliminary isothermal storage of SnO at 350 °C. In this case, the whisker yield increases by ~70 times.

It is known[29—31] that the growth of extended micro- and nanocrystals of tin oxide can be initiated on the surface of polycrystalline gold supports. We chose the tin and platinum plates as the supports and obtained, as a result, strongly branched, bent filamentary crystals with the length from tens of microns to several millimeters and the diameter from several nanometers to several microns, as well as the unique whiskers, whose length reaches several centimeters (see Fig. 5).

In the case of using the tin plates (see Fig. 5), the vaporization of metallic Sn in the cold zone produces, most likely, tin microdrops in the reaction space. They act as the "catalyst" of future crystals. The growth component formed due to SnO disproportionation in the gas phase is transferred by the nitrogen flow to a cooler zone, where the SnO_2 crystals are formed *via* the VLC mechanism. The growth of the branched crystals is due to the fact that the tin vapors present in the gas phase are condensed on the lateral walls of the boat and also on the surface of the already grown whiskers, which results in the growth of new crystals on the surface of the already formed crystals.

The use of the platinum support results in the formation of smooth and lowly branched crystals (see Fig. 5). According to published data, the Pt—Sn system contains five intermediate phases, of which Pt_3Sn and PtSn melt congruently at temperatures >1050 °C (synthesis temperature), and the Pt_2Sn_3, $PtSn_2$, and $PtSn_4$ compounds are formed *via* the peritectic reactions at 840, 745, and 522 °C, respectively. Therefore, $PtSn_x$ drops can be formed on the platinum plate surface after the condensation in the cold zone of metallic tin formed due to SnO disproportionation. It should be mentioned that the wettability in a melt—metal system is considerably higher than that at the melt—oxide boundary. Based on the EDX data for the regions where the support is not covered by the whiskers, we can conclude that a metallic tin layer is formed, in fact, on the platinum plate surface. In this connection, we can assume that during the experiment the drops are preferentially condensed on the platinum support initiating the crystal growth *via* the VLC mechanism. The congealed drops are seen on the ends of selected whiskers,

indicating in favor of this hypothesis. In addition, it has been shown by the EDX method that the platinum is virtually absent from the structure of these whiskers.

The preparation of filamentary semiconducting crystals of SnO_2 makes it possible to use the whiskers as active elements of future microsensor systems of different configuration. In the present work, the sensor properties of the synthesized whiskers were characterized by model changes in the resistance of their bundle introducing nitrogen dioxide vapors in a concentration of 0.8 ppm (Fig. 11). The maximum sensor signal is observed at low temperatures (~100 °C), although at other temperatures the signal value is quite sufficient for the creation of highly sensitive sensor devices to toxic and dangerous components of gaseous media.

From the viewpoint of fundamental research and practical significance, whiskers are among the most promising crystalline materials with the unique complex of properties. Whiskers, as a rule, have a perfect, almost ideal structure, which excludes usual dislocation mechanisms of plastic deformation and approaches the strength of whiskers to the theoretical limit. Whiskers are characterized by unique flexibility, corrosion stability, and multiple enhancement of the crystallographically induced anisotropy of the properties. They can find wide use: from strengthening fibers to nanoelectronic devices. Although filamentary crystals have been known for more than fifty years, the application of whiskers in the technology is rather lop-sided: mainly as reinforcing filaments for the creation of structure composite materials with improved mechanical properties. At the same time, using the reproducible and available experimental procedures described in this work, one can synthesize macroscopic metal oxide whiskers in a series of most important systems (Table 1). Their functional characteristics allow these whiskers to be promising for the further practical use, including the creation of new chemical current sources and sensor devices.

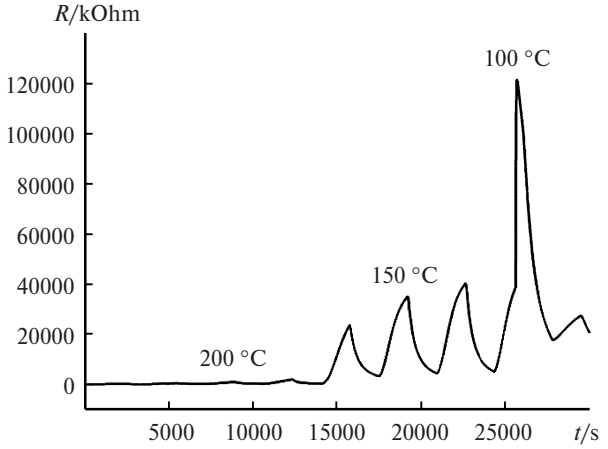

Fig. 11. Time dependence of the resistance of the SnO_2 whiskers at the periodical introduction of 0.8 ppm NO_2 at different temperatures.

This work was financially supported by the Russian Federation for Basic Research (Project Nos 07-03-00749-a and 07-08-00639-a), the Council on Grants at the President of the Russian Federation (Program of State Support for Young Russian Scientists, Grant MD-1264.2007.3), and the Federal Agency on Science and Innovations (Federal Target Scientific Technical Program).

References

1. Ch. V. Subba Reddy, J. Wei, Z. Quan-Yao, D. Zhi-Rong, C. Wen, Mho Sun-il, R. R. Kalluru, *J. Power Sources*, 2007, **166**, 244.
2. M. Malta, G. Louarn, N. Errien, R. M. Torresi, *J. Power Sources*, 2006, **156**, 533.
3. A. P. Alivisatos, *Science,* 1996, **271**, 933.
4. X. Wu, Y. Tao, L. Dong, J. Hong, *J. Mater. Chem.*, 2004, **14**, 901.

Table 1. Analytical data for the whisker samples

Method of synthesis	Phase composition (X-ray) and structural motif	Cationic composition (EDX)	Morphology (SEM)	Thermal stability (TG—DTA)	Application
Thermal decomposition (VLC)	SnO_2 — tinstone	Sn	Needle-like crystals, thickness 0.1—3 μm, length 0.1—10 mm	No decomposition is observed below temperatures of 1100 °C	Sensor
Isothermal vaporization of chloride fluxes (pedestal growth)	Framework structure of phase — structural type $Ba_6Mn_{24}O_{48}$	Ba : Mn = 1 : 4	Needle-like crystals, thickness 0.1—2 μm, length 0.1—5 mm	No decomposition is observed below temperatures 1050 °C	Catalytic and electrochemical
Hydrothermal synthesis (olation, oxolation)	Layered structure — motif of vanadium bronzes	Ba : V = 1 : 9	Needle-plate crystals, thickness less than 100 nm, length 0.1—3 mm	Decomposition at temperatures about 500 °C	Sensor, catalytic, and electrochemical

5. P. Boullay, M. Hervieu, B. Raveau, *J. Solid State Chem.,* 1997, **132**, 239.
6. E. A. Goodilin, E. A. Pomerantseva, V. V. Krivetsky, D. M. Itkis, J. Hester, Yu. D. Tretyakov, *J. Mater. Chem.*, 2005, **15**, 1614.
7. E. A. Pomerantseva, Ya. Yu. Filippov, T. L. Kulova, A. M. Skundin, A. G. Veresov, E. A. Goodilin, Yu. D. Tretyakov, *Dokl. Akad. Nauk*, 2007, **414**, 487 [*Dokl. Chem.*, 2007 (Engl. Transl.)].
8. E. A. Pomerantseva, M. G. Kozlova, D. A. Semenenko, T. S. Yashchuk, E. A. Goodilin, Yu. D. Tretyakov, *Alrternativnaya energetika i ekologiya* [*Alternative Energetics and Ecology*], 2007, **45**, No. 1, 51 (in Russian).
9. E. A. Pomerantseva, M. G. Kozlova, K. V. Didenko, A. G. Veresov, E. A. Goodilin, Yu. D. Tretyakov, *Mendeleev Commun.*, 2007, **17**, 16.
10. C. Kilic, A. Zunger, *Phys. Rev. Lett.*, 2002, **88**, 095501.
11. B. G. Lewis, D. C. Paine, *MRS Bull.*, 2000, **25**, 22.
12. H. L. Hartnagel, A. L. Dewar, A. K. Jain, C. Jagdish, *Semiconducting Transparent Thin Films*, IOP Publishing, Bristol, 1995.
13. A. Mandelis, C. Christofides, *Chemistry and Technology of Solid State Gas Sensor Devices*, Wiley, New York, 1993.
14. Wolfgan Gopel, Klaus Dieter Shierbraum, *Sensors Actuators,* 1995, 26.
15. Wenzhong Wang, Congkang Xu, Xiaoshu Wang, *J. Mater. Chem.*, 2002, 1922.
16. Wei Zhu, Wenzhong Wang, *Materials Chemistry Physics*, 2006, **99**, 127.
17. C. Xu, G. Xu, Y. Liu, X. Zhao, G. Wang, *Scr. Mater*, 2002, **46**, 789.
18. X. L. Ma, Y. Li, Y. L. Zhu, *Chem. Phys. Lett.*, 2003, **376**, 794.
19. Z. W. Pan, Z. R. Dai, Z. L. Wang, *Science*, 2001, **291**, 1947.
20. Y. Chen, X. Cui, K. Zhang, D. Pan, S. Zhang, B. Wang, J. G. Hou, *Chem. Phys. Lett.*, 2003, **369**, 16.
21. J.-S. Lee, S.-K. Sim, B. Min, K. Cho, S. W. Kim, S. Kim, *J. Cryst. Growth*, 2004, **267**, 145.
22. S. Budak, G. X. Miao, *J. Cryst. Growth*, 2006, **291**, 405.
23. Yongsheng Zhang, Ke Yua, Guodong Li, *Materials Lett.*, 2006, **60**, 3109.
24. D. V. Peryshkov, A. V. Grigor´ev, D. A. Semenenko, E. A. Goodilin, V. V. Volkov, K. A. Dembo, Yu. D. Tretyakov, *Dokl. Akad. Nauk*, 2006, **406**, 203 [*Dokl. Chem.*, 2006, **406**, No. 1, 9 (Engl. Transl.)].
25. N. Kijima, Y. Takahashi, J. Akimoto, J. Awaka, *J. Solid State Chem.*, 2005, 178, 2741.
26. W. Tang, H. Kanoh, K. Ooi, Y. Wang, *J. Mater. Sci. Lett.*, 2000, **19**, 1361.
27. S. Venkatraman, A. Manthiram, *J. Solid State Chem.*, 2004, **177**, 4244.
28. T. Kohler, T. Armbruster, E. Libowitzky, *J. Solid State Chem.*, 1997, **133**, 486.
29. C. N. R. Rao, F. L. Deepak, G. Gundiah, A. Govindraj, *Prog. Solid State Chem.*, 2003, 31.
30. Y. Xia, P. Yang, Y. Sun, Y. Wu, B. Mayers, B. Gates, Y. Yin, F. Kim, H. Yan, *Adv. Mater.*, 2003, **15**, 353.
31. M. Law, J. Goldberger, P. Yang, *Annu. Rev. Mater.*, 2004, **34**, 83.
32. L. L. Rokhlin, O. A. Bannykh, *Diagrammy sostoyaniya dvoinykh metallicheskikh sistem (Spravochnik)* [*Phase Diagrams for Binary Metallic Systems (Manual)*], Ed. N. P. Lyakishev, Vol. **3**, Book 2, Mashinostroenie, Moscow, 2000, pp. 58, 59 (in Russian).

Received January 10, 2008;
in revised form May 14, 2008